

This is the accepted manuscript made available via CHORUS. The article has been published as:

Edge states and ballistic transport in zigzag graphene ribbons: The role of SiC polytypes

A. L. Miettinen, M. S. Nevius, W. Ko, M. Kolmer, A.-P. Li, M. N. Nair, B. Kierren, L. Moreau, E. H. Conrad, and A. Tejeda

Phys. Rev. B **100**, 045425 — Published 30 July 2019

DOI: [10.1103/PhysRevB.100.045425](https://doi.org/10.1103/PhysRevB.100.045425)

Edge states and ballistic transport in zig-zag graphene ribbons: the role of SiC polytypes.

A.L. Miettinen,¹ M.S. Nevius,¹ W. Ko,² M. Kolmer,² A.-P. Li,² M. N. Nair,³ B. Kierren,⁴ L. Moreau,⁴ E.H. Conrad,^{1,*} and A. Tejada^{5,3}

¹The Georgia Institute of Technology, Atlanta, Georgia 30332-0430, USA

²Center for Nanophase Materials Sciences, Oak Ridge National Laboratory, Oak Ridge, Tennessee 37831, USA

³Synchrotron SOLEIL, L'Orme des Merisiers, Saint-Aubin, 91192 Gif sur Yvette, France

⁴Institut Jean Lamour, CNRS-Universit  de Lorraine, 54506 Vandoeuvre les Nancy, France

⁵Laboratoire de Physique des Solides, Universit  Paris-Sud, CNRS, UMR 8502, F-91405 Orsay Cedex, France

Zig-zag edge graphene sidewall ribbons grown on 6H-SiC $\{11\bar{2}n\}$ facet walls are ballistic conductors. It is assumed that graphene sidewall ribbons grown on 4H-SiC $\{11\bar{2}n\}$ facets would also be ballistic. In this work, we show that SiC polytype indeed matters; ballistic sidewall graphene ribbons only grow on 6H SiC facets. 4H and 4H-passivated sidewall graphene ribbons are diffusive conductors. Detailed photoemission and microscopy studies show that 6H-SiC sidewalls zig-zag ribbons are metallic with a pair of n-doped edge states associated with asymmetric edge terminations. In contrast, 4H-SiC zig-zag ribbons are strongly bonded to the SiC; severely distorting the ribbon's π -bands. H_2 -passivation of the 4H ribbons returns them to a metallic state but show no evidence of edge states in their photoemission derived band structure.

I. INTRODUCTION

Epitaxial graphene (EG) is graphene grown from silicon carbide (SiC).¹ When grown on the SiC(0001) (Si-face), it has a known orientation relative to the SiC substrate and can be grown as uniform single layers. The bottom-up growth of EG ribbons on facets of patterned SiC(0001) shallow trenches (known as "sidewall" graphene) was proposed as a viable route towards graphene electronics,^{1,2} circumventing patterned exfoliated graphene's lithographic limits on ribbon width and edge disorder.³⁻⁸ This is because the edges of EG ribbons are defined entirely by the orientation of the SiC(0001) pre-growth trenches. Trenches parallel to the SiC $\langle 1\bar{1}00 \rangle$ direction produce zig-zag (ZZ) edges ribbons on the SiC step facets [see Fig. 1]. Armchair (AC) edge ribbons grow on steps parallel to the SiC $\langle 11\bar{2}0 \rangle$ direction.

An exciting work found that ZZ-edge sidewall ribbons grown on 6H-SiC substrates were room temperature ballistic conductors using 2- and 4-point measurements.^{9,10} The current development of ballistic devices on modern 4H-substrate has implicitly assumed that ZZ-edge graphene grown on 4H- and 6H-SiC would be the same. However, attempts to measure the band structure of 4H ZZ-edge sidewall graphene found no evidence of metallic graphene on the sidewall despite exploring growth conditions up to the melting point of the SiC trenches.¹¹ Thin metallic graphene strips were found on the (0001) surface near the step edges of the facet, just not on the sidewalls.¹² These conflicting results lead to the unresolved question: what structural or growth variables affect ZZ-edge sidewall graphene formation? In this work, we show that the dominant factor in ZZ-edge sidewall graphene growth is the SiC polytype, not the growth method. Angle resolved photoemission (ARPES) measurements show that sidewall ZZ-ribbons with metallic

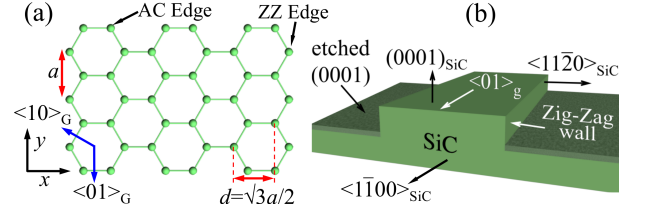


FIG. 1. (a) Graphene lattice. (b) The pre-growth etched SiC(0001) step geometry to grow ZZ-edge sidewall graphene. The distance between ZZ rows is $d = \sqrt{3}a/2$, $a = 2.462\text{\AA}$.

π -bands readily grow on 6H-SiC but not on 4H-SiC. On 4H-SiC, the graphene's π -bands are severely distorted by graphene-Si bonds to the SiC facets; similar to the graphene-substrate bonding that makes the first graphene layer on SiC(0001) semiconducting.¹³⁻¹⁶ H_2 -passivation of 4H-ribbons restores the π -band's metallic character. The 6H ZZ-edge ribbons have two flat bands below the Fermi Energy (E_F). These bands are consistent with the nearly flat edge states predicted for ZZ-ribbons with asymmetric edge terminations.¹⁷ The broken symmetry of the 6H-edge states has the potential to be used in spin valve devices.¹⁷ 4H-passivated ribbons show no evidence of n-doped edge states or a significant bandgap. 2-point resistance measurements on 6H sidewall ZZ-ribbons are independent of the ribbon length, consistent with ballistic transport while both 4H and passivated 4H ribbons' resistance are strong functions of the ribbon length, consistent with diffusive conductance.

Figure 2(a) shows 2-point resistance (R_{2p}) measurements on different sidewall ZZ-ribbons. The figure shows that R_{2p} for 6H-ribbons is independent of probe separation with a value of $R_{2p} \sim h/e^2$, i.e., they are ballistic conductors like previously measured 6H ZZ-ribbons.¹⁸ 4H and 4H-passivated ribbons on the other hand show dif-

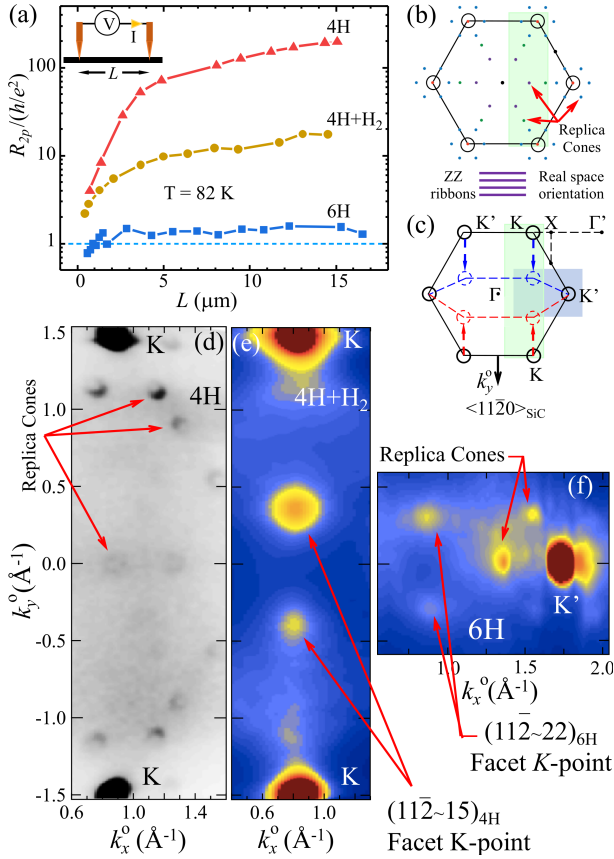


FIG. 2. (a) The 2-point resistance, R_{2p} , normalized by h/e^2 vs probe separation for three different ZZ-ribbons: 4H, 4H+H₂-passivated and 6H. (b) and (c) Graphene (0001) BZ. Dots in (b) are 6×6 replica cone positions. (c) The compressed graphene BZs (dashed lines and circles) of the $\{11\bar{2}n\}$ (blue) and $\{\bar{1}\bar{1}2n\}$ (red) plotted in the (0001) coordinate frame. (d), (e), and (f) are ARPES constant E cuts for three ZZ-sidewall samples ($E - E_F = -0.09$ eV and $h\nu = 36$ eV). (d) A cut for 4H ZZ-ribbons [green area in (b) and (c)] showing intensity from both (0001) and (6×6) replica cones. (e) Same as (d) but after H₂-passivation. Intensity from $\{11\bar{2} \sim 15\}_{4H}$ facets Dirac cones become visible. (f) A cut for 6H ZZ-ribbons [blue area in (c)]. The $\{11\bar{2} \sim 22\}_{6H}$ graphene facets cones are marked.

fusive resistance curves. The resistance of 4H and 4H-passivated ribbons is linear in L . Note that Fig. 2(a) is plotted on a log scale so the linear dependence is obscured [See Supplementary Material for details]. Similarly, dI/dV measurements of the different sidewall graphene ribbons show that 4H-ribbons are gapped semiconductors [see Supplementary material]. As we now discuss, the reason for these transport differences is the nature of the graphene-substrate interaction on the different SiC polytypes.

II. EXPERIMENTAL

Samples were prepared starting from a polished SiC(0001) sample from Cree Inc. Trenches with $\{11\bar{2}0\}$ facet walls are formed by e-beam patterning lines on SiC followed by plasma etching to produce well defined 25-30 nm deep trenches 400 nm apart over a 1 mm² area. The (0001) trench tops are 200 nm wide. The samples are grown by first using an anneal step to stabilize the step structure.¹¹ This is followed by a rapid high temperature growth step. The rapid heating grows the graphene quickly thus limiting step melting by preventing Si evaporation through an essentially impervious graphene layer; similar to carbon capping methods.¹⁹ Details of the process are found in the Supplementary Material and in Ref. [11]. The ribbons are grown in a confinement-controlled sublimation furnace.²⁰ The process causes the surface of the step to reorganize into a complicated set of equilibrium facets and simultaneously grow sidewall graphene. Graphene does not grow well on the SiC(0001) plasma-etched trench bottoms.¹² This limits graphene growth to the step walls and a small strip on the (0001) surface at the step edge. To H₂-passivate the post-graphene growth 4H-SiC trenches, samples were heated at 900 °C for 1 hour in an H₂ furnace ($P_{H_2} \sim 800$ mtorr). ARPES measurements were done on the high resolution Cassiopée beamline. The line has a total measured instrument resolution of $\Delta E < 12$ meV using a Scienta R4000 detector with a $\pm 15^\circ$ acceptance at $\hbar\omega = 36$ eV. Samples were mounted on a 3-axis cryogenic manipulator. The STM experiments were carried out in an ultra-high vacuum setup with a base pressure in the low 10^{-10} mbar range using a commercial low-temperature Omicron microscope that was modified to minimize capacitive coupling [see Supplemental material and Ref. [21].

Scanning tunneling spectroscopy (STS) and two-probe transport measurements were made on two different cryogenic four-probe scanning tunneling microscope (4P-STM) systems; one operated at 82 K and the other at 4.6 K.^{22,23} All measurements were done under UHV condition ($< 10^{-10}$ torr). Because the graphene sidewall samples were exposed to the air after growth, they were cleaned prior to measurement by annealing in the UHV chamber at 300-500 °C for a several hours before STM measurements. See Supplemental Material for more details.

III. RESULTS

A. Structure

Figure 2 also compares ARPES intensity cuts, $I(\vec{k}^\circ, E)$ at fixed binding energy ($BE = E - E_F$), for three different ZZ-ribbon arrays: 4H-, 4H-H₂-passivated, and 6H-ribbons. \vec{k}° is in the (0001) surface plane. The facet walls are sufficiently well ordered after graphene growth

so that the 40 μm diameter ARPES beam, averaging over ~ 100 sidewalls, give a good ensemble average of the ribbon band structure.²⁴ The ARPES intensity is related to the 2D-band dispersion $E(\vec{k}_{\parallel})$ where \vec{k}_{\parallel} is in the plane of the local surface. Because of the ARPES beam size, bands from both the (0001) and the opposing $\{11\bar{2}n\}$ and $\{\bar{1}\bar{1}2n\}$ facets are simultaneously measured [see Fig. 2(c)]. Any Dirac cones from graphene on the facets appear shifted in k_y^o relative to the cones of the (0001) Brillouin zone (BZ) [see Fig. 2(c)].²⁴ When we attempt to grow ZZ-ribbons on 4H trenches, the $I(\vec{k}_{\parallel}, E)$ map in Fig. 2(d) only shows K-point cones and 6th- order replica cones associated with the reconstructed graphene-SiC(0001) surface [see Fig. 2(b)].^{14,25} There is no evidence of rotated Dirac cones from graphene on the facets. Either no graphene has grown or the graphitic carbon that did grow is bonded strongly enough to the SiC facet to significantly distort the graphene's π -bands.¹² The lack of Dirac cones on 4H-sidewalls persists up to temperatures where the SiC steps melt.¹¹ As we now show, 4H ZZ-ribbon cones from facet graphene appear once the graphene-SiC bonding is broken.

To demonstrate that graphene is strongly bonded to the 4H sidewalls, we have H_2 -passivated the 4H-ribbons in Fig. 2(d). H_2 -passivation is known to break the graphene-substrate silicon bonds; turning a semiconducting graphene film on SiC(0001)^{13,14} to a metallic film.²⁶ Figure 2(e) shows the same ARPES map as Fig. 2(d) but after H_2 -passivation. The passivated sample shows that a set of modified Dirac cones appearing along the line between the two K-points of the (0001) surface. As shown in the schematic BZ in Fig. 2(c), these cones are from graphene on the tilted facets. We note that the different facet cone intensities are due to ARPES matrix element effects caused by the different angles between the photon polarization vector and the opposing facet normals. The angle between the (0001) plane and the facet normal, θ_F , is found from the k_y^o positions of the facet cones and from their asymmetry. The asymmetry is a result of ARPES matrix element effects [See Supplementary Material for details].^{27,28} We find $\theta_F = 23.6 \pm 0.5^\circ$, corresponding to $\{11\bar{2} \sim 15\}_{4\text{H}}$ planes.

While graphene-Si bonding causes 4H ZZ-sidewall graphene to be non-metallic, graphene grown on 6H-SiC $\{11\bar{2}n\}_{6\text{H}}$ facets is naturally metallic. Figure 2(f) shows a partial ARPES map for ZZ-ribbons grown on 6H-SiC. Unlike 4H-ribbons, Dirac cones from 6H-facets appear after growth without passivation. The 6H-facets have $\theta_F = 24 \pm 0.5^\circ$, corresponding to graphene ribbons on $\{11\bar{2} \sim 22\}_{6\text{H}}$ planes. The fact that the π -bands are observed without H-passivation demonstrates that 4H ZZ-sidewall graphene is bonded very differently to the substrate compared to 6H-ribbons. We believe that the graphene-substrate interaction on the 4H facet is analogous to the buffer graphene-substrate interaction where the graphene becomes semiconducting because of graphene-Si bonds. Our 4H ZZ-graphene results imply

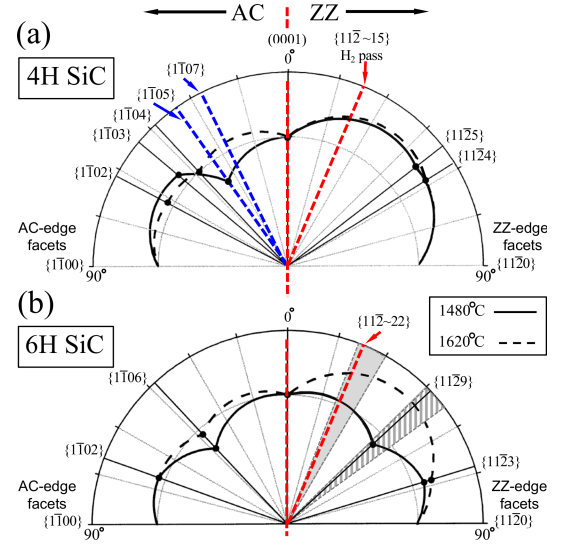


FIG. 3. $F(\theta)$ plots for (a) 4H- and (b) 6H-SiC based on calculated (black lines) and experimental (dots) growth rates for two temperatures [modified from Ref. [29]]. Both 4H and 6H SiC polytypes have pronounced minima for $\{1\bar{1}0n\}$ facets, indicating stable AC steps. In contrast, stable ZZ $\{11\bar{2}n\}$ facets only exists on 6H-SiC, the $\{1129\}_{6\text{H}}$. Blue dashed lines mark the known stable 4H AC facet after graphene growth [from Refs. [24 and 30]]. Red dashed lines mark the stable ZZ-facets from this work. Gray shaded area in (b)) were estimated by STM in Ref. [9] Grey hatched area shows a range of angles where disordered ZZ-sidewall graphene grows for deep trenches.⁹

that there are more Si dangling bonds available to interact with the sidewall graphene on 4H- compared to 6H-facets. More structural work will be required to understand the atomic structure of 4H and 6H facets before this conjecture can be quantified..

While it is clear that the SiC polytype matters for graphene sidewall growth, it was certainly assumed that the two bulk terminated, non-polar, 4H- and 6H-SiC $\{11\bar{2}n\}$ planes would be very similar and lead to similar ZZ-graphene sidewall ribbons. It turns out, however, that their energetics are known to be very different. Figure 3 shows the surface free energy as a function of angle, $F^{\text{SiC}}(\theta)$, for both 4H and 6H SiC [modified from Ref. [29]]. The plots include facet angles for AC $\{1\bar{1}0n\}$ and ZZ $\{11\bar{2}n\}$ planes. Minima in $F(\theta)$ usually correspond to stable facets. Since well defined minima are calculated and measured for AC $\{1\bar{1}0n\}$ planes on both 4H- and 6H-SiC, there are stable AC facets on both polytypes. In contrast, $F^{\text{SiC}}(\theta)$ for ZZ-facets in Fig. 3 predicts that only the 6H-SiC polytype will have a stable facet; the $\{1129\}_{6\text{H}}$ at $\theta_F = 47.5^\circ$. Clearly the polytype matters in the facet stability of 4H- and 6H-AC and ZZ-facet walls.

Of course we do not expect $F^{\text{SiC}}(\theta)$ for bare SiC to be the same as $F^{\text{G+SiC}}(\theta)$ when the facets have graphene on them. There are apparent differences in $F(\theta)$ after graphene growth. Experimental high resolution trans-

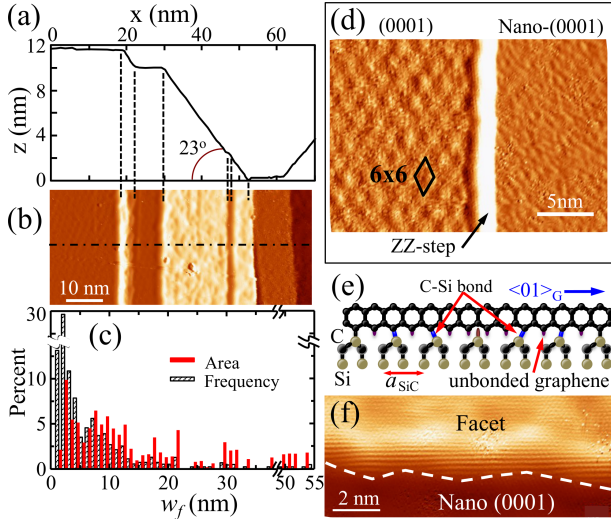


FIG. 4. (a) Post graphene growth profile near the bottom of a 25 nm high 6H ZZ-edge steps. (b) A dI/dV image of the step in (a). (c) Histogram of 250 facet widths plotted by both relative frequency and areal coverage. (d) dI/dV image comparison of the macroscopic (0001) surface and an adjacent nano (0001) terrace separated by a ZZ-edge step. (e) Bonding geometry of a ZZ-edge ribbon to a commensurate bulk terminated $(6\sqrt{3} \times 6\sqrt{3})R30^\circ$ SiC surface. (f) Atomic resolution image of a facet-(0001) boundary showing the chiral meandering (dashed line) of graphene at the step edge.

mission electron microscopy (HRTEM) measurements³⁰ and ARPES²⁴ on graphene growth on 4H-SiC sidewalls find that the $(1\bar{1}07)$, not the $(1\bar{1}05)$, is the dominant observed facet. Figure 3 simply shows that it is not unreasonable that there can be differences in ZZ-sidewall graphene grown on the two polytypes. In this work, the stable facet walls when ZZ-sidewall graphene grows are 23.6° and 24° for 4H- and 6H-SiC, respectively. From an energetics point of view, however, the 6H $\{11\bar{2} \sim 22\}_{6H}$ planes must have a lower free energy than the 4H $\{11\bar{2} \sim 15\}$ counterpart because the 4H-SiC surface prefers to bond to graphene to lower its energy.

Unlike AC-steps where a single $(1\bar{1}07)$ facet covers $\sim 70\%$ of the step area,³⁰ 6H ZZ-steps have a complicated facet structure.^{9,18} The ZZ-steps consist of many $\{11\bar{2} \sim 22\}_{6H}$ -(0001) plane pairs [see Figs. 4(a)]. The $\{11\bar{2} \sim 22\}_{6H}$ facets have a broad width distribution as shown in Fig. 4(c). The histogram gives an average 6H facet width of $\bar{w}_f \sim 6 \pm 8$ nm with a high number of 1-2 nm facets. The important question is how the graphene ribbon width-distribution, $N(W_r)$, is related to the facet width distribution $N(w_f)$, i.e. does the facet graphene flow onto and over the (0001) nano-terraces as a continuous very wide ribbon (like a carpet draping over a staircase) or does the facet graphene terminate somewhere on an adjacent (0001) terraces so that $N(W_r) \sim N(w_f)$? As we will show, both STM and ARPES find that the graphene ribbon width is similar to the facet width.

Figure 4(b) shows a dI/dV map of the step profile in

Fig. 4(a). The fact that the facets are bright compared to the (0001) nano-terraces indicates that there is a discontinuity in the electronic structure of the graphene on facet and the semiconducting graphene that is known to grow on the nano-terraces.³⁰ These results suggest that the facet graphene either terminates into the SiC(0001) surface or transitions into a semiconducting form of graphene on the (0001) nano surface. In either case, the results suggest that graphene is a metallic ribbon of width proportional to the facet width. As we will show below, this statement is supported by the ARPES data.

B. Electronic Structure

Both the 6H- and 4H-passivated ZZ ribbons are sufficiently ordered to allow detailed area-averaged band measurement. Figure 5(a) shows the 6H ribbons' band intensity for k_x^f along the $K'K''$ direction of the $(11\bar{2} \sim 22)$ facet plane. The 6H ZZ-ribbon's π^- and π^+ bands' momentum and widths were determined from Lorentzian fits to momentum distribution curves (MDC); $I(k_x^f, BE)$ at fixed BE [See Supplemental material]. In this paper, we will refer to integrated π -band intensity as the integrated Lorentzian intensity from these fits. The π -band positions (marked by circles) show a distorted Dirac cone. For $BE < -0.4$ eV, the bands have an asymmetric dispersion with a larger band velocity, v_F , for the π^+ band ($v_F^+/v_F^- \sim 1.7$). Both tight binding (TB) and ab initio models predict this asymmetry for narrow ribbons.^{31,32}

For $BE > -0.4$ eV, the MDC fits show a consistent apparent spitting of π -bands [see Figs. 5(a) and (b)]. While the splitting appears unusual, it is a result of a distribution of the valance band maximum (VB_m) positions (k_x^m) from a ribbon width distribution on the facets that contains a large number of sub 5 nm parallel ribbons. To demonstrate this, we use a TB model for the ribbon's band structure. In this model the $n=0$ subband is due to the ribbon edges (the edge state). The k_y^f wavevector for this state is imaginary, localizing the wavefunction to the edges for $k_c \leq k_x^f \leq X$, where the critical momentum k_c depends on ribbon width, W_r .³²

$$k_c = \frac{2}{a} \arccos \left[\frac{1}{2} \frac{W}{W + d} \right] \quad (1)$$

d is the spacing between ZZ chains [see Fig. 2]. In both TB and first principle models, the top of the $n=1$ subband corresponds to the ribbon's VB_m.³¹ To a very good approximation, VB_m occurs at $k_x^m \sim k_c$ [See Supplemental material]. For ribbons with $W \gg d$, VB_m occurs at the K-point. Ribbons with $W \sim d$ have VB_m shifted to higher k_x . Figure 5(b) compares the calculated k_c position from Eq. (1) using the experimental $N(w_f)$ distribution in Fig. 4(c). We have convoluted the calculated k_x with a $\Delta k_x = 0.05 \text{ \AA}^{-1}$ window consistent with the measured Lorentzian width. The calculated VB_m-distribution reproduces the asymmetric ARPES intensity

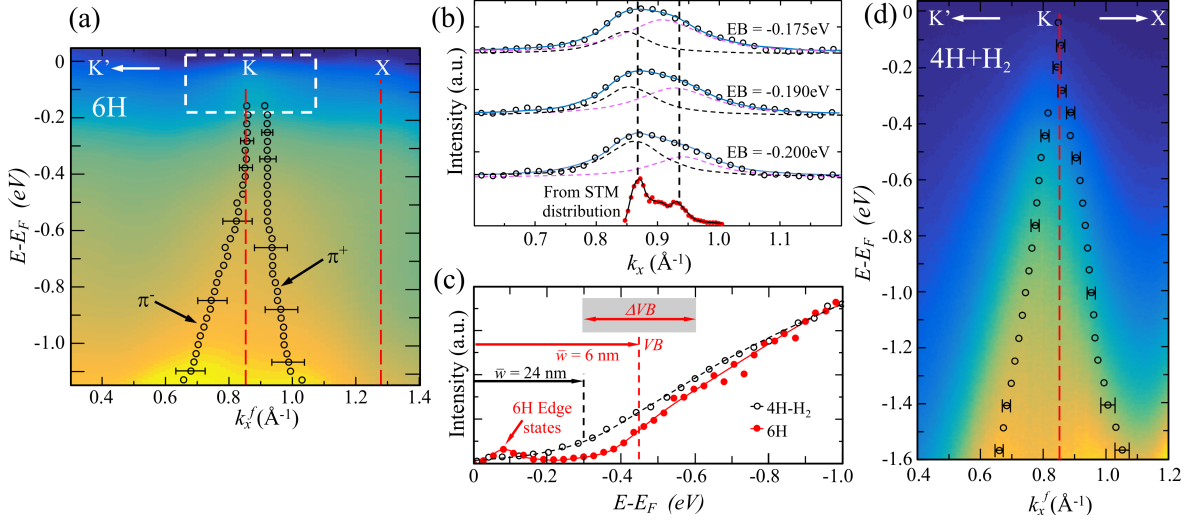


FIG. 5. (a) ARPES measures bands of 6H-ZZ sidewall ribbons along the $K'\Gamma'$ direction (parallel to the ZZ-edge). $T_{\text{sample}} = 100\text{ K}$. k_x^f is in the plane of the $(11\bar{2}\sim 22)$ facet. Circles (\circ) mark the band positions. (b) Typical MDC fits showing the π -bands asymmetry for $\text{BE} > -0.4\text{ eV}$. Solid red circles show the predicted asymmetry from the measured facet $N(w_f)$ distribution and Eq. (1). (c) Integrated π -band intensity for 6H (red circles) and H_2 -passivated 4H ribbons (black circles). Red arrows mark the estimated valance band edge and width from 6H STM ribbon $N(w_f)$. (d) ARPES bands from H_2 -passivated 4H-ZZ ribbons along the $K'\text{KX}$ direction (30 nm steps). k_x^f is in the $(11\bar{2}\sim 15)_{4\text{H}}$ plane.

very well. This can only happen if $N(W_r) \sim N(w_f)$, i.e. $W_r \sim w_f$.

The equality of the facet and graphene ribbon widths also explains the VB's intensity decay and the π -bands' momentum broadening for $\text{BE} > -0.4\text{ eV}$. To show this, we use the calculated $n = 0$ subband energy splitting, $\Delta^\circ(W_r)$, at the K-point in the GW approximation;³¹

$$\Delta^\circ \approx A/(W_r + \delta), \quad (2)$$

where $A = 38\text{ eV}\text{\AA}$ and $\delta = 16\text{ \AA}$.³¹ Roughly, VB_m is $\sim 0.5\Delta^\circ$ below E_F for neutral ribbons. Using the STM measured w_f -distribution for $N(W_r)$ in Eq. (2) gives the average position of the valance band to be $\text{VB}_m = 0.44\text{ eV}$ with a distribution of $\Delta\text{VB}_m = 0.24\text{ eV}$. These values are marked on the plot of the 6H-ZZ ribbon π -band intensity, $I(\text{BE})$, in Fig. 5(c). They are in good agreement with the experimental intensity that has a broad decay centered around an inflection point near $\text{BE} = -0.5\text{ eV}$.

Finally, the π -band Δk_x^f broadening near the inflection point of the integrated 6H π -band intensity [$\text{BE} \sim -0.45\text{ eV}$ in Fig. 5(c)] is $\sim 0.17\text{ \AA}^{-1}$; three times the broadening for BE closer to E_F . The larger Δk_x^f near VB_m is caused by overlapping sub-band energies from ribbons with different widths. Again, area-averaged ARPES contains intensity from a distribution of sub-bands, $n(W_r)$ (shifted up and down in BE) that leads to an apparent Δk_x -broadening of the π -bands. To estimate Δk_x , we assume a linear π -band dispersion, $E = \hbar\tilde{c}k$, where \tilde{c} is the average measured band velocity of the π -bands. If the apparent band broadening is

$\Delta E \approx \delta\Delta^\circ(W_r)$, then Δk_x^f is given by:

$$\Delta k_x^f \approx \frac{\Delta^\circ(\bar{w}_f)\Delta\bar{w}_f}{\hbar\tilde{c}(\bar{w}_f + \delta)}, \quad (3)$$

where we have again assumed that $w_f = W_r$. Using the measured STM values for \bar{w}_f , gives $\Delta k_x^f = 0.14\text{ \AA}^{-1}$; in good agreement with the measure value. In short, the π -band's shape, splitting, and Δk_x^f broadening are all consistent with 4H ZZ-ribbons having a width approximately equal to the $(11\bar{2}\sim 22)$ facet widths.

What distinguishes ZZ-ribbons from AC-ribbons is the existence of a ZZ-edge state.³² Because these states are localized near the ribbon edges, their spectral weight is low. Nevertheless, we find two states, ϵ_1 and ϵ_2 near E_F in Fig. 5(a) that we can identify as edge states. The states are seen more clearly in Fig. 6(a) and (b). Energy distribution curve, EDC, $I(\text{BE} : k_x^f)$ at fixed k_x^f , show that the states are essentially dispersionless along $\text{KK}'\Gamma'$ [see Fig. 6(a)]. EDCs near K in Fig. 6(b) show that the BE of the two states are: $\epsilon_1 = -56$ and $\epsilon_2 = -103\text{ meV}$. Their energy width is 58 meV ; essentially the expected thermal broadening for the $T = 100\text{ K}$ sample. We identify these bands as ZZ edge states associated with asymmetric edge terminations. This assignment follows from three observations: (i) Their intensity and perpendicular broadening along $\text{K} < k_y^f < \text{X}$ is consistent with predictions, (ii) the states do not disperse in either k_x^f or k_y^f , and (iii) the bands are narrow in E .

Figures 6(c) and (d) show that the average ϵ_1 and ϵ_2 intensity decreases for $k_x^f > \text{K}$ while their perpendicular band width, Δk_y^f , increases $k_x^f > \text{K}$. These are the expected trends for edge states in a TB model for ZZ-

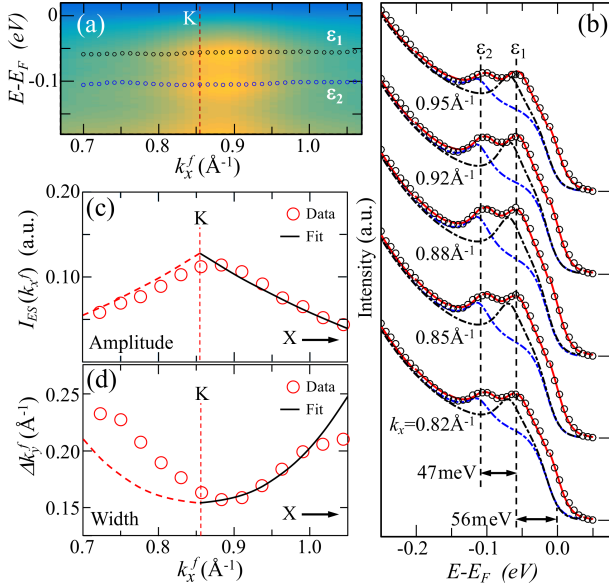


FIG. 6. (a) Close up of 6H-ZZ sidewall ribbon band structure near E_F [dashed box in Fig. 5(a)] showing flat bands, ϵ_1 and ϵ_2 . Circles \circ mark the peak positions from EDCs fits. (b) Sample EDCs near E_F in (a) (\circ are data). A two Lorentzian (dashed black and blue lines) plus background and Fermi-Dirac cut off fit is shown (red Solid line). (c) and (d) are ϵ_1 and ϵ_2 average intensity and Δk_y^f width, respectively, vs k_x^f . Solid and dashed lines are TB estimates described in the text.

ribbons. Using symmetric ZZ edges, the TB edge state's charge density, $\rho(y)$, is completely localized at the edge when $k_x^f = \pi/a$ (the 1D X-point). At lower k_x^f , it becomes more delocalized until at the K-point ($k_x^f = 2\pi/3a$) $\rho(y)$ is uniform perpendicular to the edge.³² Therefore, the edge state band width, $\Delta k_y^f \sim 2\pi/\Delta y$, is largest at X and smallest at K. Furthermore the edge state intensity, $I_{ES}(k_x^f)$, is proportional to $\cos(k_x^f a/2)$.³² Thus $I_{ES}(k_x^f)$ is a maximum at K and decreases as k_x^f approaches the X-point. The TB estimates [See Supplemental Material] for $I_{ES}(k_x^f)$ and Δk_y^f , are plotted in Figs. 6(c) and (d). Note that Δk_y^f has been convoluted with a 0.16 \AA window to match the experimental minimum at K. Dashed lines in Figs. 6(c) and (d) are mirrored versions of the solids lines about K.

While there are similarities between the 6H ribbon edge states and TB predictions, there are significant differences. First, the measured edge states are narrow in energy ($\Delta E = 58 \text{ meV}$). Since the edge state splitting, Δ° , from symmetrically terminated ribbons depends on W_r , we would expect ϵ_1 and ϵ_2 to have a significant ΔE due to $N(W_r)$. From Eq. 2, the STM w -distribution would give $\Delta E \sim 0.5 \text{ eV}$; 9 times larger than measured. Furthermore, the ϵ_1 and ϵ_2 bands are flat while theoretical models for symmetric edge terminations predict a strong dispersion along the K'KX direction, regardless of whether or not they are anti-ferromagnetic (AF) or ferromagnetically (F) coupled.^{31,33–36} Asymmetric terminations models, on the other hand, give rise to nearly flat

bands near E_F .^{17,37} In particular sp^2 termination on one edge and sp^3 on the other, gives rise to nearly flat bands through the entire 1D BZ whose energies are essentially independent of the ribbon width.¹⁷ In other words, our edge states are not from symmetric ribbons.

The fact that the ARPES data points to asymmetric edges is not unexpected. Based on HRSTEM images of 4H-SiC AC-steps, the ribbons terminate into semiconducting buffer graphene on the macroscopic (0001) surface through sp^2 C-C bonds.³⁰ At the step bottom, the ribbon terminates by either C-Si sp^3 bonds to the substrate SiC (Type I termination in Fig. 7 (a)) or by an intermediate sp^2 C-C bond to buffer graphene on (0001) nano-facets (Type II in Fig. 7 (b)). The asymmetric Type I termination is more complicated than Fig. 7 indicates. While the ribbon-buffer edge is commensurate and ordered, the C-Si sp^3 edge is incommensurate with the SiC [see Figs. 4(e)].¹⁶ The aperiodic C-Si sp^3 bonding leads to $>60\%$ bond defects with the edge-carbon either unbonded or re-hybridized in some complicated way. This fraction can be larger since the actual (0001) surface has 20% less Si than a bulk terminated surface.^{38,39} The edge structure is also complicated by the patterned step edges being slightly rotated with respect to the SiC, $\phi \sim 2-2.5^\circ$. This leads to a chirality in the step edges as the graphene terminate into the (0001) planes [see Fig. 4(f)]. Line defects in graphene are also known to lead to flatter band over the entire zone compared to H-terminated ribbons.⁴⁰ Regardless of the details of the asymmetric C-Si sp^3 edges, the narrow energy widths and dispersionless character of the observed ϵ_1 and ϵ_2 bands are consistent with edge states from asymmetric edge terminations in the sidewall SiC system.

While Type II ribbons resemble a wave-guide geometry with metallic graphene ribbon bonded to a semiconducting graphene on both edges, their terminations are also asymmetric. This is because buffer graphene on macroscopic (0001) and nano (0001) terraces are structurally and electronically different. Only the macroscopic (0001) surface shows the typical (6 \times 6) reconstruction [see Fig. 4(d)].⁴¹ Furthermore, dI/dV data clearly show a bias dependent contrast difference between macroscopic and nano (0001) surfaces [See Supplemental Material]. How this waveguide affects transport is an open question. Regardless, Type II ribbon can be thought of as an asymmetric Type I ribbon with a more complicated structure between sp^2 and sp^3 edges.

Data on 4H H_2 -passivated ribbons implies a very different ribbon geometry compared to 6H-ribbons. Figure 5(d) shows the band structure from the passivated 4H ZZ-ribbons. The cut through the BZ is the same cut as in Fig. 5(a). The flat edge state bands below E_F are not seen in the passivated 4H sample. We would expect a change in the edge states because the hydrogen treatment would not only transform semiconducting buffer graphene to metallic on all (0001) terraces,⁴² it would also break any C-Si bonds at the Type I edges and hydrogenate a large fraction of unbonded carbon along

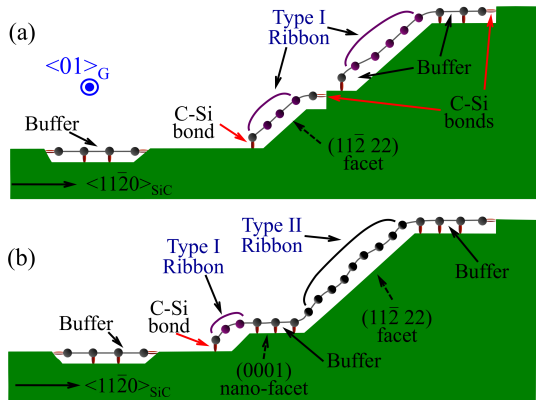


FIG. 7. Two edge terminated 6H ZZ-ribbons. Functionalized (buffer) graphene is represented by grey circles bonded to the SiC. (a) Type I ribbons terminated by C-C bonds into buffer graphene on one side and C-Si bonds to the substrate on the other side. (b) A Type II termination with metallic graphene terminated on both sides by C-C bonds into buffer graphene.

the edges. While H_2 -passivation can p-dope graphene by ~ 100 meV and shift the states above E_F where they would not be visible in ARPES,²⁶ the diffusive conductance measured in transport [see Fig. 2(a)] suggest that there are either no edge states or that any finite size gap is too small to electronically isolate a particular subband.

Besides the missing edge states, there are other differences in the 4H-passivated π -bands compared to 6H-ribbons. Unlike 6H-ribbons, the H_2 -passivated 4H-ribbon's π^- and π^+ -bands are nearly symmetric about the K -point with the same band velocity found in macroscopic sheets, $v_F \sim 1 \times 10^6$ m/sec. The k_x^f -position of VB_m is essentially at the K -point and there is no evidence of a Δk_x^f splitting of the π -bands. This rules out any significant number of sub 5 nm ribbons. If a VB_m exists, it must occur at $BE \gtrsim -0.3$ eV. According to Eq. 2, that BE would imply a 4H-ribbons width of $\bar{W}_{4H} > 24$ nm. It is clear that either the 4H-step is approximately a single $(11\bar{2} \sim 15)$ facet or the sidewall graphene that grows is only terminated at the top and bottom of the step.

IV. CONCLUSIONS

To summarize, we demonstrate that metallic ZZ-edge epitaxial graphene ribbons only grow on the $\{11\bar{2}, 22\}_{6H}$ facets of the 6H-SiC polytype. While graphene does

grow on the 4H polytype, it is bonded to the facet walls in a way that heavily modifies the graphene π -bands, similar to why the first graphene layer on SiC(0001) is semiconducting because of graphene-SiC bonds. The non-metallic 4H-ribbons can be turned metallic by H_2 -passivation that breaks the graphene-sidewall bonds.

STM, STS, and ARPES measurements show that 6H facet walls consist of multiple $\{11\bar{2}, 22\}_{6H}$ -(0001) nano-plane pairs. These pairs appear electronically isolated from each other and give rise to a width distribution where more than $> 80\%$ of the ribbons are less than 12 nm wide ($> 50\%$ between 1-3 nm). ARPES measurements find two non-dispersing states 56 and 103 meV below E_F that are identified as ZZ-ribbon edge states. These states' dispersion, width, and intensity dependence on in-plane momentum indicate that they originate from asymmetrically terminated ZZ-edges. The lack of an observed crossing of the two states suggests that they are anti-ferromagnetically aligned on opposite edges of the ribbon. Transport measurements shows that these 6H ZZ-ribbons are ballistic conductors up to at least $16 \mu m$.

Unlike 6H sidewall ribbons, ARPES shows that the 4H sidewall ribbons appear to be a single wide sheet over the entire 4H facet. Both the passivated and unpassivated 4H sidewall ribbons show no evidence of n-doped edge states. 2-point transport measures for both the 4H and H_2 -passivated 4H sidewall ribbons indicate that they are diffusive conductors. It is possible that non-local probe measurements on 4H-ribbons may demonstrate ballistic transport even though there is no metallic graphene on the facets. It is known that narrow metallic graphene ribbons form on the (0001) surface near the facet step edge.¹² Conduction through these ribbons cannot be discriminated against using non-local gates. Also, graphene grown on shallow trenches, less than 5 nm deep, may interact differently with the SiC facet because of the ribbon's finite radius of curvature; preventing bonding to the facet and allowing them to remain metallic. These two possibilities remains to be systematically tested.

Acknowledgments This research was supported by the National Science Foundation under Grant No. DMR-1401193 (EHC). ALM acknowledges a travel grant from the School of Physics at Georgia Tech. A.T. acknowledges support from the Agence Nationale de la Recherche (France) under contract CoRiGraph. A portion of the work (multiprobe STM) was conducted at the Center for Nanophase Materials Sciences (CNMS), which is a DOE Office of Science User Facility.

* email: edward.conrad@physics.gatech.edu

¹ C. Berger, Z. Song, T. Li, X. Li, A. Y. Ogbazghi, R. Feng, Z. Dai, A. N. Marchenkov, E. H. Conrad, P. N. First, and W. A. de Heer, The Journal of Physical Chemistry B **108**, 19912 (2004).

² K. Nakada, M. Fujita, G. Dresselhaus, and M. S. Dresselhaus, Phys. Rev. B **54**, 17954 (1996).

³ SprinkleM, RuanM, HuY, HankinsonJ, M. Rubio-Roy, ZhangB, WuX, BergerC, and W. A. de Heer, Nat Nano **5**, 727 (2010).

⁴ K. Todd, H.-T. Chou, S. Amasha, and D. Goldhaber-Gordon, Nano Letters **9**, 416 (2009), pMID: 19099454,

<http://dx.doi.org/10.1021/nl803291b>.

- ⁵ K. A. Ritter and J. W. Lyding, *Nature Materials* **8**, 235 EP (2009).
- ⁶ M. Y. Han, J. C. Brant, and P. Kim, *Phys. Rev. Lett.* **104**, 056801 (2010).
- ⁷ E. R. Mucciolo, A. H. Castro Neto, and C. H. Lewenkopf, *Phys. Rev. B* **79**, 075407 (2009).
- ⁸ F. Sols, F. Guinea, and A. H. C. Neto, *Phys. Rev. Lett.* **99**, 166803 (2007).
- ⁹ J. Baringhaus, F. Edler, and C. Tegenkamp, *Journal of Physics: Condensed Matter* **25**, 392001 (2013).
- ¹⁰ J. Baringhaus, M. Ruan, F. Edler, A. Tejada, M. Sicot, I. Taleb, A.-P. Li, Z. Jiang, E. H. Conrad, C. Berger, C. Tegenkamp, and W. A. de Heer, *Nature* **506**, 349 (2014).
- ¹¹ M. S. Nevius, *Improved growth, ordering, and characterization of sidewall epitaxial graphene nanoribbons*, Ph.D. thesis, Georgia Institute of Technology (2016).
- ¹² M. S. Nevius, F. Wang, C. Mathieu, N. Barrett, A. Sala, T. O. Mente, A. Locatelli, and E. H. Conrad, *Nano Letters* **14**, 6080 (2014), pMID: 25254434, <http://dx.doi.org/10.1021/nl502942z>.
- ¹³ K. V. Emtsev, F. Speck, T. Seyller, L. Ley, and J. D. Riley, *Phys. Rev. B* **77**, 155303 (2008).
- ¹⁴ M. S. Nevius, M. Conrad, F. Wang, A. Celis, M. N. Nair, A. Taleb-Ibrahimi, A. Tejada, and E. H. Conrad, *Phys. Rev. Lett.* **115**, 136802 (2015).
- ¹⁵ M. N. Nair, I. Palacio, A. Celis, A. Zobelli, A. Gloter, S. Kubsky, J.-P. Turmaud, M. Conrad, C. Berger, W. de Heer, E. H. Conrad, A. Taleb-Ibrahimi, and A. Tejada, *Nano Letters* **17**, 2681 (2017), pMID: 28345926, <http://dx.doi.org/10.1021/acs.nanolett.7b00509>.
- ¹⁶ M. Conrad, F. Wang, M. Nevius, K. Jinkins, A. Celis, M. Narayanan Nair, A. Taleb-Ibrahimi, A. Tejada, Y. Garreau, A. Vlad, A. Coati, P. F. Miceli, and E. H. Conrad, *Nano Letters* **17**, 341 (2017), pMID: 27981850, <http://dx.doi.org/10.1021/acs.nanolett.6b04196>.
- ¹⁷ X. Deng, Z. Zhang, G. Tang, Z. Fan, and C. Yang, *Carbon* **66**, 646 (2014).
- ¹⁸ J. Aprozanz, S. R. Power, P. Bampoulis, S. Roche, A.-P. Jauho, H. J. W. Zandvliet, A. A. Zakharov, and C. Tegenkamp, *Nature Communications* **9**, 4426 (2018).
- ¹⁹ C.-Y. Lu, J. A. Cooper, T. Tsuji, G. Chung, J. R. Williams, K. McDonald, and L. C. Feldman, *IEEE Transactions on Electron Devices* **50**, 1582 (2003).
- ²⁰ W. A. de Heer, C. Berger, M. Ruan, M. Sprinkle, X. Li, Y. Hu, B. Zhang, J. Hankinson, and E. Conrad, *Proc. Nat. Acad. of Sci.* **108**, 16900 (2011).
- ²¹ C. Didiot, A. Tejada, Y. Fagot-Revurat, V. Repain, B. Kierren, S. Rousset, and D. Malterre, *Phys. Rev. B* **76**, 081404 (2007).
- ²² T.-H. Kim, Z. Wang, J. F. Wendelken, H. H. Weitering, W. Li, and A.-P. Li, *Review of Scientific Instruments* **78**, 123701 (2007), <https://doi.org/10.1063/1.2821610>.
- ²³ A.-P. Li, K. W. Clark, X.-G. Zhang, and A. P. Baddorf, *Advanced Functional Materials* **23**, 2509 (2013).
- ²⁴ J. Hicks, A. Tejada, A. Taleb-Ibrahimi, M. S. Nevius, F. Wang, K. Shepperd, J. Palmer, F. Bertran, P. Le Fevre, J. Kunc, W. A. de Heer, C. Berger, and E. H. Conrad, *Nat Phys* **9**, 49 (2013).
- ²⁵ A. Bostwick, T. Ohta, T. Seyller, K. Horn, and E. Rotenberg, *NATURE PHYSICS* **3**, 36 (2007).
- ²⁶ C. Riedl, C. Coletti, T. Iwasaki, A. A. Zakharov, and U. Starke, *Phys. Rev. Lett.* **103**, 246804 (2009).
- ²⁷ E. L. Shirley, L. J. Terminello, A. Santoni, and F. J. Himpsel, *Phys. Rev. B* **51**, 13614 (1995).
- ²⁸ A. Bostwick, T. Ohta, J. L. McChesney, K. V. Emtsev, T. Seyller, K. Horn, and E. Rotenberg, *New Journal of Physics* **9**, 385 (2007).
- ²⁹ N. Nordell, S. Karlsson, and A. Konstantinov, *Materials Science and Engineering: B* **61-62**, 130 (1999).
- ³⁰ I. Palacio, A. Celis, M. N. Nair, A. Gloter, A. Zobelli, M. Sicot, D. Malterre, M. S. Nevius, W. A. de Heer, C. Berger, E. H. Conrad, A. Taleb-Ibrahimi, and A. Tejada, *Nano Letters* **15**, 182 (2015).
- ³¹ L. Yang, C.-H. Park, Y.-W. Son, M. L. Cohen, and S. G. Louie, *Phys. Rev. Lett.* **99**, 186801 (2007).
- ³² K. Wakabayashi, K.-i. Sasaki, T. Nakanishi, and T. Enoki, *Science and Technology of Advanced Materials* **11**, 54504 (2010).
- ³³ Y.-W. Son, M. L. Cohen, and S. G. Louie, *Phys. Rev. Lett.* **97**, 216803 (2006).
- ³⁴ L. Pisani, J. A. Chan, B. Montanari, and N. M. Harrison, *Phys. Rev. B* **75**, 064418 (2007).
- ³⁵ J. Jung and A. H. MacDonald, *Phys. Rev. B* **79**, 235433 (2009).
- ³⁶ O. V. Yazyev, *Reports on Progress in Physics* **73**, 056501 (2010).
- ³⁷ G. Lee and K. Cho, *Phys. Rev. B* **79**, 165440 (2009).
- ³⁸ J. D. Emery, B. Detlefs, H. J. Karmel, L. O. Nyakiti, D. K. Gaskill, M. C. Hersam, J. Zegenhagen, and M. J. Bedzyk, *Phys. Rev. Lett.* **111**, 215501 (2013).
- ³⁹ M. Conrad, J. Rault, Y. Utsumi, Y. Garreau, A. Vlad, A. Coati, J.-P. Rueff, P. F. Miceli, and E. H. Conrad, *Phys. Rev. B* **96**, 195304 (2017).
- ⁴⁰ S. Dutta and K. Wakabayashi, *Scientific Reports* **5**, 11744 EP (2015).
- ⁴¹ C. Riedl, U. Starke, J. Bernhardt, M. Franke, and K. Heinz, *Phys. Rev. B* **76**, 245406 (2007).
- ⁴² J. Sforzini, L. Nemec, T. Denig, B. Stadtmüller, T.-L. Lee, C. Kumpf, S. Soubatch, U. Starke, P. Rinke, V. Blum, F. C. Bocquet, and F. S. Tautz, *Phys. Rev. Lett.* **114**, 106804 (2015).